Article

Silver-Platinum Hollow Nanoparticles as Labels for Colorimetric Lateral Flow Assay

Jinfeng Zhou [1], Shikuan Shao [1], Zhiyuan Wei [1], and Xiaohu Xia [1,2,*]

[1] Department of Chemistry, University of Central Florida, Orlando, FL 32816, USA
[2] NanoScience Technology Center, University of Central Florida, Orlando, FL 32816, USA
* Correspondence: xiaohu.xia@ucf.edu
Received: 23 September 2024; Revised: 7 November; Accepted: 12 November 2024; Published: 18 November 2024

Abstract: Colorimetric lateral flow assay (CLFA) has been a widely recognized point-of-care testing technology over the past few decades. Driven by the increasing demand in various biomedical applications, it is urgently needed to develop CLFAs with high sensitivities and low costs. In this work, we report a type of CLFA that relies on unique colorimetric labels—silver-platinum hollow nanoparticles (Ag-Pt HNPs). The Ag-Pt HNPs possess intrinsic enzyme-like catalytic activities, providing the Ag-Pt HNP-based CLFA with strong color signal and thus a high sensitivity. Meanwhile, the Ag-Pt HNPs have hollow interiors and are mainly composed of less expensive silver, making the Ag-Pt HNP-based CLFA cost-effective. Using prostate-specific antigen (PSA) as a model disease biomarker, the Ag-Pt HNP-based CLFA achieved a high sensitivity with a detection limit at the low picogram-per-milliliter level. Potential application of the CLFA in clinical diagnosis was demonstrated by detecting PSA from human serum samples.

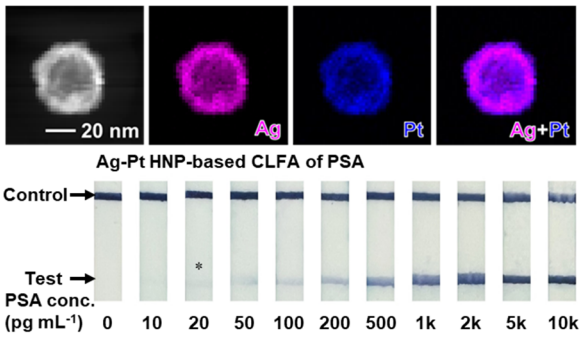

Keywords: hollow nanoparticles; lateral flow assay; catalysis; biomarker; detection

1. Introduction

Over the past few decades, lateral flow assays (LFAs) have been widely recognized and used as an accessible point-of-care (POC) technique due to their end-user-friendly, simple, rapid, and cost-effective natures [1,2]. Among various types of LFAs, colorimetric LFAs (CLFAs) stand out owing to their straightforward readouts, which provide visible test results without the need for additional equipment to stimulate or read signals [2]. This characteristic makes CLFAs particularly appealing for use in resource-limited settings [3]. Nevertheless, a significant drawback of CLFAs is their relatively low detection sensitivities compared to other laboratory tests. Conventional CLFAs typically use solid gold nanoparticles (Au NPs) with an overall spherical shape as labels (i.e., nanoscale particles pre-functionalized with bioreceptors that are responsible for specifically producing a visible signal in the test/control lines of a CLFA test strip) [1,4]. The color signal in conventional Au NP-based CLFAs originates from the plasmonic activities of Au NPs, which are intrinsically confined by the size of particles [5]. In general, small Au NPs generate limited colorimetric signals. Larger Au NPs or Au NP aggregates, however, can impede the mobility of the labels in the test strip [6]. Such a reduction of label mobility results in non-specific retention of labels in the membrane of test strip, leading to prolonged assay time and elevated background signals. In addition, bulky labels also cause steric hindrance that reduces the binding efficiency of the bioreceptors to analytes [7]. Because of the size effects, Au NPs of approximately 40 nm in diameter are widely used in conventional CLFAs [8–10].

To address these limitations, recent advancements have introduced a novel approach to substantially enhance the sensitivity of CLFAs. This approach employs platinum-group metal nanoparticles (PGM NPs) with peroxidase-like catalytic activities as labels, which are also known as “peroxidase mimics” or “artificial peroxidase” [11,12]. For example, in recent studies [8,13,14], conventional Au NPs were coated with Pt or Ir to form Au-Pt or Au-Ir

core-shell NPs. The Pt or Ir shells endowed the nanoparticles with high peroxidase-like activities, which could generate intense color signals by catalyzing the oxidation of chromogenic substrates (e.g., 3,3′,5,5′-tetramethylbenzidine (TMB) and 3,3′-diaminobenzidine (DAB) [15]) in the test region of CLFA. Through this catalytic process, these PGM NPs can generate a much stronger color signal than conventional Au NP-based labels that rely on intrinsic plasmonic activities, thereby significantly improving the sensitivity of CLFA. Despite their advantages, PGM NPs are precious and costly materials. Most of the reported PGM NPs used in CLFAs were solid particles [16], where only the surface layers contributed to catalytic activity [16,17]. In a sense, the underutilized PGM inside the solid particles causes extra materials costs.

In this work, we report a type of hollow PGM-based nanoparticles as labels for CLFA, namely silver-platinum hollow nanoparticles (Ag-Pt HNPs). The Ag-Pt HNPs were synthesized through galvanic replacement between silver nanoparticles (Ag NPs) and Pt^{2+} ions. The Ag-Pt HNPs possess hollow interiors and are mainly made of less expensive Ag, greatly reducing the materials cost of PGM. Using prostate-specific antigen (PSA) as a model analyte, we have demonstrated that the Ag-Pt HNP-based CLFA could offer a high sensitivity with a limit of detection (LOD) over 20-fold lower than the LOD of conventional Au NP-based CLFA. The design of labels in this work greatly enhances both the sensitivity and cost-effectiveness of CLFA, aligning with the Affordable, Sensitive, Specific, User-friendly, Rapid/Robust, Equipment-free, and Deliverable (ASSURED) criteria suggested by the World Health Organization (WHO) for POC diagnostics [18].

2. Materials and Methods

2.1. Materials and Reagents

Silver nitrate ($AgNO_3$, ≥99.0%), gold(III) chloride trihydrate ($HAuCl_4 \cdot 3H_2O$, ≥99.9%), sodium citrate dihydrate (≥99%), L-ascorbic acid (≥99%), potassium tetrachloroplatinate(II) ($K_2PtCl_4 \cdot 6H_2O$, 98%), hydrogen peroxide solution (H_2O_2, 30 wt % in H_2O), 3,3′,5,5′-tetramethylbenzidine (TMB, >99%), sodium acetate (NaOAc, ≥99%), acetic acid (HOAc, ≥99.7%), sodium borohydride ($NaBH_4$), prostate-specific antigen (PSA) from human semen, bovine serum albumin (BSA, ≥98%), potassium phosphate monobasic (KH_2PO_4, ≥99%), sodium phosphate dibasic (Na_2HPO_4, ≥99%), potassium chloride (KCl, ≥99%), sodium chloride (NaCl, ≥99.5%), sodium azide (NaN_3, ≥99.5%), sodium carbonate (Na_2CO_3, ≥99.5%), human serum (male AB plasma), TMB substrate solution for membranes, Tween 20, and NP 40 were all purchased from Sigma Aldrich (St. Louis, MS, USA). Monoclonal mouse anti-human PSA detection antibody (referred to as "anti-PSA DAb") and polyclonal rabbit anti-human PSA capture antibody (referred to as "anti-PSA CAb") were obtained from Abcam plc (Waltham, MA, USA). Polyclonal goat anti-mouse IgG antibody and Pierce protein concentrator (PES, 10K MWCO, 0.5 mL) were obtained from Thermo Fisher Scientific, Inc (Suwanee, GA, USA). The patient serum sample with PSA was purchased from Boca Biolistics LLC, Pompano Beach, Florida. Nitrocellulose (NC) membrane, glass fiber membrane, and absorbent pad were obtained from Cytiva. Polyvinyl chloride (PVC) backing card was obtained from DCN Diagnostics. All materials and reagents were used as received without further purifications and treatments. All aqueous solutions were prepared using deionized (DI) water with a resistivity of 18.2 MΩ·cm.

2.2. Instrumentations

The steady-state kinetic assays were recorded by an Agilent Cary 60 UV-vis spectrophotometer (Santa Clara, CA, USA). Transmission electron microscopy (TEM) images were taken using a JEOL 1011 microscope operated at 200 kV (Peabody, MA, USA). High-angle annular dark-field scanning TEM (HAADF-STEM) and energy dispersive X-ray (EDX) mapping images were taken using a FEI 200 kV Titan Themis scanning transmission electron microscope (Hillsboro, OR, USA). The concentrations of Au, Ag, and Pt ions (which were obtained from the digestion of nanoparticles by aqua regia) were determined using an inductively coupled plasma mass spectroscopy (ICP-MS, Thermo Scientific iCAP RQ, Waltham, MA, USA). These concentrations could be converted to the particle concentrations of Au NPs and Ag-Pt HNPs once the particle sizes and shapes had been resolved by TEM analyses. X-ray photoelectron spectroscopy (XPS) was performed on a Physical Electronics 5400 ESCA spectrometer system (Chanhassen, MN, USA). Fourier transform infrared spectroscopy (FT-IR) analyses were performed using a Shimadzu IRSpirit Infrared Spectrometer (Tampa, FL, USA). The lateral flow assay test strips were prepared by a ZX1000 Dispensing Platform and a CM4000 Guillotine Cutter (BioDot Inc.,Irvine, CA, USA). The pH values of all buffer solutions were measured by an Oakton pH 700 benchtop meter. Photographs of strips were taken using a Canon EOS 80D digital camera (Huntington, NY, USA).

2.3. Synthesis of Ag NPs and Au NPs

The ~40 nm, citrate-capped Ag NPs (see Supplementary Figure S1) were synthesized using a two-step growth method [19]. First, the silver seed solution was prepared as follows: 12 mL of sodium citrate (SC) aqueous solution (0.25%, *w*/*v*) was added to a 50 mL round-bottom flask with a condenser and heated to boiling in an oil bath under magnetic stirring. Next, 270 μL of $AgNO_3$ (10 mg mL^{-1}) solution and 300 μL of freshly prepared $NaBH_4$ (1.0 mg mL^{-1}) solution were sequentially injected using a pipet. The reaction mixture was kept boiling and stirring for 30 min until the solution color became bright yellow. After that, the silver seed solution as the product was cooled to room temperature and stored in dark for future use. In the second step, the ~40 nm Ag NPs were synthesized using a seed-mediated growth with minor modifications [20]. Briefly, 1.0 mL of preformed silver seed solution was diluted to 35 mL with water in a 100 mL round-bottomed flask and heated to 80 °C in an oil bath under magnetic stirring. After 10 min, 256 μL of SC solution (1%, *w*/*v*), 256 μL of L-ascorbic acid solution (1%, *w*/*v*), and 256 μL of $AgNO_3$ solution (1%, *w*/*v*) were sequentially injected using a pipet with a time interval of ~1 min. The reaction was terminated after 30 min. The ~40 nm Ag NPs as final products were cooled to room temperature and stored in dark for future use.

The citrate-capped Au NPs with an average diameter of ~40 nm (see Supplementary Figure S2) were prepared according to our previously reported procedures [8].

2.4. Synthesis of Ag-Pt HNPs

The Ag-Pt HNPs were synthesized based on the galvanic replacement reaction between the above-mentioned ~40 nm Ag NPs as sacrificial templates and K_2PtCl_4, according to published protocols with some modifications [21,22]. In a standard synthesis, 10 mL of ~40 nm Ag NPs was added to a 50 mL round-bottomed flask and preheated to 80 °C in an oil bath under magnetic stirring. Then, 160 μL of K_2PtCl_4 solution (0.005%, *w*/*v*) was injected into the flask at a rate of 8 μL min^{-1} using a syringe pump. After completing injection of the K_2PtCl_4 solution, the reaction mixture was kept stirring at 80 °C for 10 min to allow reaction to complete. The Ag-Pt HNPs as final products were collected by centrifugation and eventually redispersed in 1.0 mL of water for future use.

2.5. Steady-State Kinetic Assays

All steady-state kinetic assays were performed at room temperature in cuvettes with a path length (l) of 1.0 cm using 0.2 M NaOAc/HOAc buffer (pH = 4.0) as the reaction buffer [23,24]. A final particle concentration at 8.6×10^{-13} M for Ag-Pt HNP suspension was used for all kinetic measurements. Note that the particle concentrations in this work were quantified using a combination of ICP-MS analysis and TEM imaging (see the Instrumentations section for details). After the addition of the nanoparticles to the reaction solution containing 2.0 M H_2O_2 and TMB of different concentrations, the absorbance of the reaction solution at 653 nm for each sample was immediately measured as a function of time using a UV-vis spectrophotometer for 1 min (interval = 3 s). The "absorbance vs. time" plots were then used to derive the slope at the initial point ($Slope_{Initial}$) of each reaction by performing the first derivation using Origin 2019 software. The initial reaction velocity (v) was calculated by $Slope_{Initial}/(\varepsilon_{oxTMB\text{-}653\ nm} \times l)$, where $\varepsilon_{oxTMB\text{-}653\ nm}$ is the molar extinction coefficient of oxidized TMB at 653 nm ($\varepsilon_{oxTMB\text{-}653\ nm} = 3.9 \times 10^4\ M^{-1}\ cm^{-1}$) [23,24]. The plots of v against TMB concentrations were fitted using nonlinear regression of the Michaelis-Menten equation. The apparent kinetic parameters were calculated based on the Michaelis-Menten equation: $v = V_{max} \times [S]/(K_m + [S])$, where V_{max} is the maximal reaction velocity, [S] represents the concentration of TMB substrate, and K_m is the Michaelis constant. V_{max} could be obtained from the double reciprocal plot (or Lineweaver-Burk plot) [25]. Finally, the catalytic constant (K_{cat}, which is defined as the maximum number of colored products generated per second per single nanoparticle) can be obtained from the equation: $K_{cat} = V_{max}/[E]$, where [E] is the catalyst concentration (i.e., 8.6×10^{-13} M).

2.6. Conjugation of Antibodies to Nanoparticles

A non-covalent method was used to conjugate Ag-Pt HNPs to antibodies [8,16]. Specifically, 2 μL of anti-PSA DAb (2 mg mL^{-1}) was added to 100 μL of as-prepared Ag-Pt HNP suspension. After incubating at room temperature for 30 min, the mixture was put in a refrigerator overnight at 4 °C. Subsequently, 10 μL of blocking solution (10 mM phosphate buffered saline (PBS) buffer, pH 7.4, containing 10% BSA) was added to the mixture and incubated for 1 h. The final products (i.e., Ag-Pt HNP-anti-PSA DAb conjugates) were collected by centrifugation, washed twice by PBS, and redispersed in 100 μL of PBS solution containing 5% BSA, 0.5% NP40,

and 0.05% NaN_3 for future use. The same conjugation procedure was used for functionalizing Au NPs with anti-PSA DAb, which yielded Au NP-anti-PSA DAb conjugates as the final products.

2.7. Fabrication of CLFA Test Strips

The Ag-Pt HNP-based CLFA test strips were fabricated according to our previously reported protocol with minor modifications [8]. Specifically, a ZX1000 dispensing platform and a CM4000 Guillotine Cutter (BioDot Inc. Irvine, CA, USA) were used for the test strip fabrication. As shown in Figure 3A, a test strip comprises five main components: an absorbent pad, a PVC backing card, a nitrocellulose (NC) membrane with test and control lines, a sample pad, and a conjugate pad. The backing card and absorbent pad were used without pretreatment. The sample pad was prepared by immersing the glass fiber membrane in PBS solution containing 5% BSA, 0.5% NP40, and 0.05% NaN_3, followed by drying at room temperature for 4 h. The conjugate pad was prepared by dispensing Ag-Pt HNP-anti-PSA DAb conjugates onto the glass fiber membrane at a rate of 25 μL cm^{-1} using the ZX1000 dispensing platform, followed by drying at room temperature for 2 h. The NC membrane with test and control lines was prepared by spotting anti-PSA CAb (1.1 mg mL^{-1} in PBS buffer containing 0.05% NaN_3, which was pre-concentrated with a Pierce protein concentrator) at the test line region and anti-mouse IgG (1.2 mg mL^{-1} in PBS containing 0.05% NaN_3) at the control line region using a ZX1000 dispensing platform at the spray rate of 1.0 μL cm^{-1}. The interval between the test and control lines was set to 8.0 mm. Finally, the sample pad, the conjugate pad, the NC membrane, and the absorbent pad were pasted to the PVC backing card with a 2 mm overlap between each component. The assembled sheets were then cut into 3 mm wide strips. The resultant Ag-Pt HNP-based CLFA strips were stored in refrigerator at −20 °C under dry conditions for future use.

The procedure for preparing Au NP-based CLFA strips was the same as that for the Ag-Pt HNP-based CLFA strips, except that Ag-Pt HNP-anti-PSA DAb conjugates were substituted with the Au NP-anti-PSA DAb conjugates of the same particle concentration.

2.8. Detection of PSA by CLFA

The assay procedure of Ag-Pt HNP-based CLFA for PSA detection involves two steps: a sample loading step, which is a standard and routine procedure for CLFA, and a TMB substrate treatment step for color signal development [8,14]. Specifically, in the first step, 100 μL of PSA standard or human serum sample was loaded onto the sample pad of an Ag-Pt HNP-based CLFA strip using a pipet. Note, the serum samples were pre-diluted 2 folds by assay buffer (i.e., 1% BSA in PBS containing 0.05% Tween 20). The CLFA strip was then kept at room temperature for ~10 min until the liquid flow stopped. In the second step, a PBS solution containing 5% BSA, 0.5% NP40, and 0.05% NaN_3 was dropped to the sample pad using a pipet to wash away the excess Ag-Pt HNP-anti-PSA DAb conjugates in the NC membrane. Then, TMB substrate treatment process was applied according to the following procedure: the Ag-Pt HNP-based CLFA strip was immersed in a plastic centrifuge tube containing 1.5 mL of TMB substrate solution (i.e., a mixture containing 0.9 mL of TMB substrate solution for membrane, 0.3 mL of 1.0 M NaOAc/HOAc buffer, pH 4.0, and 0.3 mL of 1.0 M H_2O_2) at room temperature. After ~5 min of incubation, photograph of the CLFA strip was taken using a digital camera. For quantitative analysis, all photographs were imported into a computer and converted to 8-bit grayscale images using Adobe Photoshop software. The arithmetic mean of the pixel intensity in the test line region was measured as the color signal intensity [14].

The assay procedure for the Au NP-based CLFA of PSA was the same as the procedure for Ag-Pt HNP-based CLFA, except for the omission of TMB substrate treatment step.

3. Results and Discussion

3.1. Synthesis and Characterization of Ag-Pt HNPs

Ag-Pt HNPs were synthesized through galvanic replacement reaction between the ~40 nm Ag NPs as sacrificial templates and K_2PtCl_4 (see the Experimental section) [21]. Figure 1A,B shows typical transmission electron microscopy (TEM) images of the Ag-Pt HNPs at low- and high-magnifications, respectively. It can be observed that the Ag-Pt HNPs had good uniformities in terms of both shape and size. The Ag-Pt HNPs were of overall spherical shape with a hollow interior. By randomly analyzing 100 particles in the TEM images, the average outer diameter of the particles was measured to be 42.4 nm and their average wall thickness was measured to be 5.2 nm. In addition to morphology (i.e., size and/or shape), we also examined the elemental composition of these nanoparticles. The energy-dispersive X-ray (EDX) mapping images of an individual Ag-Pt HNP (see Figure 1C) revealed that elemental Ag and Pt co-exist in the particles in the form of Ag-Pt alloy, which is consistent with our

previous study [21]. The overall molar ratio of Ag to Pt in the Ag-Pt HNPs was quantified to be roughly 4:1 by inductively coupled plasma mass spectrometry (ICP-MS) analysis. This result suggests that the nanoparticles were primarily made of less expensive silver, ensuring a low material cost relative to those solid nanoparticles of pure PGMs.

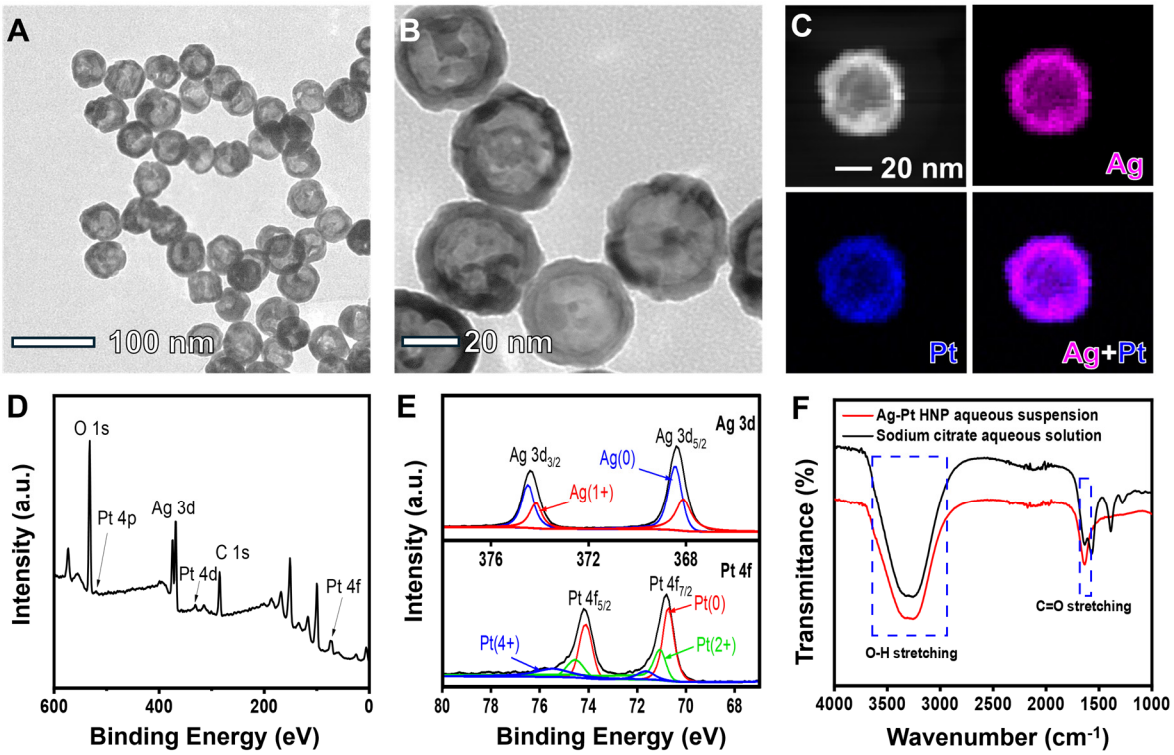

Figure 1. Morphological, structural, and compositional analyses of the Ag-Pt HNPs. (**A**,**B**) TEM images at low and high magnifications, respectively. (**C**) EDX mapping image of an individual particle (magenta = Ag, blue = Pt). (**D**) XPS survey spectrum. (**E**) High-resolution XPS spectra of the Ag 3d and Pt 4f regions shown in (**D**). (**F**) FT-IR spectra taken from an aqueous suspension of Ag-Pt HNPs and an aqueous solution of sodium citrate.

Surface chemistry of the Ag-Pt HNPs was characterized by X-ray photoelectron spectroscopy (XPS) and Fourier transform infrared spectroscopy (FT-IR). Figure 1D shows a full XPS spectral survey recorded from the Ag-Pt HNPs. The observation of peaks for Ag 3d, Pt 4p, Pt 3d, and Pt 4f confirmed that the nanoparticles were composed of Ag and Pt elements. The high-resolution XPS spectra of the Ag 3d and Pt 4f regions (Figure 1E) revealed that the Ag-Pt HNPs were mainly composed of zero-valent Ag(0) and Pt(0). The co-existence of relatively small amounts of oxidized metal atoms was presumably because of surface oxidations (e.g., by dissolved oxygen in nanoparticle suspensions) [26]. Notably, as shown by the full spectral scan (Figure 1D) and the high-resolution spectra (see Supplementary Figure S3), C 1s and O 1s peaks were observed, hinting at the absorbance of citrate on the surface of Ag-Pt HNPs. This assumption was confirmed by the FT-IR results (see the red spectrum in Figure 1F). Specifically, the peak observed at ~1600 cm^{-1} was representative of the C=O stretch. The broad peak between 3100 and 3400 cm^{-1} was attributed to be from the O−H stretch. These characteristic peaks of citrate on nanoparticle surface were overall consistent with the peaks observed from pristine citrate (black spectrum in Figure 1F). These FT-IR analyses along with the XPS data confirmed the absorption of citrate on the surface of Ag-Pt HNPs. Note that this result implies that the citrate acting as a colloidal stabilizer on initial Ag NP templates was retained on particle surface after the galvanic replacement reaction. The capping of citrate on particle surface allows for convenient conjugation of the Ag-Pt HNPs with antibodies through attractive electrostatic interactions [27,28].

It is worth noting that all these characterization data demonstrate that the Ag-Pt HNPs had a similar size and shape and the same surface ligand as the ~40 nm citrate-capped Au NPs—a type of widely used label in the CLFA industry [9,29]. Such similarities facilitate a direct and reasonable comparison of the Ag-Pt HNPs and Au NPs in CLFA performance.

3.2. Catalytic Activities

The peroxidase-like catalytic activities of Ag-Pt HNPs were assessed using the oxidation of TMB (a typical peroxidase substrate) by H_2O_2 as a model catalytic reaction. This catalytic reaction yielded a blue product (i.e., oxidized TMB [30]) with maximal absorbance at ~653 nm, which could be easily tracked and quantified by a UV-vis spectrophotometer (see Supplementary Figure S4). It is worth noting that in addition to TMB, 2,2′-azino-bis(3-ethylbenzothiazoline-6-sulfonic acid) diammonium salt (ABTS), 3,3′-diaminobenzidine (DAB), and o-phenylenediamine (OPD) are commonly used peroxidase substrates that can yield blue/green-, brown-, and orange-colored products, respectively [31]. Nevertheless, in the context of application in CLFA, the catalytic products from the peroxidase substrates are preferred to meet the following expectations: (i) The color should be easily distinguished from that of the samples (e.g., red for whole blood samples); (ii) The products can be rendered to be insoluble by a precipitator to avoid being washed away by the liquid flow in the test strip; and (iii) the products exhibit minimal toxicities to human and environment. Taking all these into consideration, TMB is the optimal choice among all the peroxidase substrates.

To quantify the catalytic efficiency of Ag-Pt HNPs, an apparent steady-state kinetic assay was conducted, in which the particle concentration of Ag-Pt HNPs (E) was fixed at 8.6×10^{-13} M (details are provided in the Experimental section). Note that the catalytic efficiency is measured by a parameter—catalytic constant (K_{cat}) that is defined as the maximum number of colored molecules produced per second per catalyst [23,24]. Figure 2A shows the Michaelis-Menten curve, which was obtained by nonlinear fitting of the initial reaction velocity (v) at varying TMB concentrations. This curve was further transformed into a double reciprocal plot (Figure 2B), from which a maximum reaction rate (V_{max}) of 9.6×10^{-7} M s^{-1} was derived. Therefore, the catalytic constant K_{cat} was determined to be 1.1×10^{6} s^{-1}, according to the equation $K_{cat} = V_{max}/[E]$. Notably, the K_{cat} of Ag-Pt HNPs as peroxidase mimics is several orders of magnitude higher than that of horseradish peroxidase (HRP, a typical natural peroxidase with a $K_{cat} = 4.0 \times 10^{3}$ s^{-1}) [24]. It is worth mentioning that the molar extinction coefficient of ~40 nm citrate-capped Au NPs is approximately at the level of 10^{10} M^{-1} cm^{-1} as reported in previous studies [8,32]. In comparison, the equivalent molar extinction coefficient of the Ag-Pt HNPs (which is defined as the total light extinction of color products yielded at catalytic reaction time t = 5 min [8]) is estimated to be at the regime of 10^{13} M^{-1} cm^{-1}, based on their catalytic efficiency. In a sense, the color signal from the catalytic Ag-Pt HNPs (with a short reaction time of 5 min) is orders of magnitude stronger than that from conventional plasmonic Au NPs.

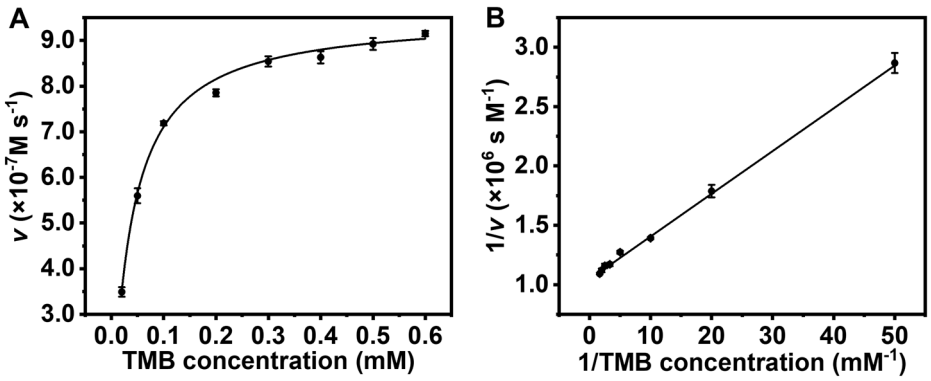

Figure 2. Kinetic assays of the Ag-Pt HNPs as catalysts for the oxidation of TMB by H_2O_2. The initial reaction velocity (v) was measured from 0.2 M HOAc/NaOAc buffer solution (pH 4.0) containing 2.0 M H_2O_2, 8.6×10^{-13} M Ag-Pt HNPs, and TMB of various concentrations at room temperature. (**A**) Plot of v against TMB concentration. (**B**) Double-reciprocal plot derived from the data in (**A**). Error bars denote the standard deviations of three independent measurements.

3.3. Application in CLFA

As illustrated in Figure 3A, the Ag-Pt HNPs were applied as labels to CLFA. Prostate-specific antigen (PSA, a biomarker for recurrence of prostate cancer [33]) was detected as a model disease biomarker to demonstrate the potential application of Ag-Pt HNP-based CLFA in medical diagnostics. After capturing the Ag-Pt HNP-antibody conjugates in the test and control line regions of the test strip, a simple TMB substrate treatment process was applied, which took only ~5 min and was operated at room temperature. Details of the CLFA assembly and assay procedures are provided in the Experimental section. It should be mentioned that instead of directly dropping the substrate solution onto the test and control lines as reported in previous studies [8,14], in this work we immersed the test strip in a substrate solution hosted in a plastic tube. Such a modification of the substrate treatment procedure

ensures good assay reproducibility and relatively low background at the expense of extra substrate solution, which is inexpensive [34]. Notably, the Ag-Pt HNPs display a visible color (gray) due to their plasmonic activities. Nevertheless, this color is significantly weaker than the color signal produced from the nanoparticles-medicated catalytic reaction [8]. Therefore, the color signal in the test and control lines of Ag-Pt HNP-based CLFA test strip is primarily from the catalytic reaction products (i.e., oxidized TMB). For comparison, conventional CLFA using ~40 nm citrate-capped Au NPs (see Supplementary Figure S2) as labels was fabricated using the same antibodies and materials as Ag-Pt HNP-based CLFA.

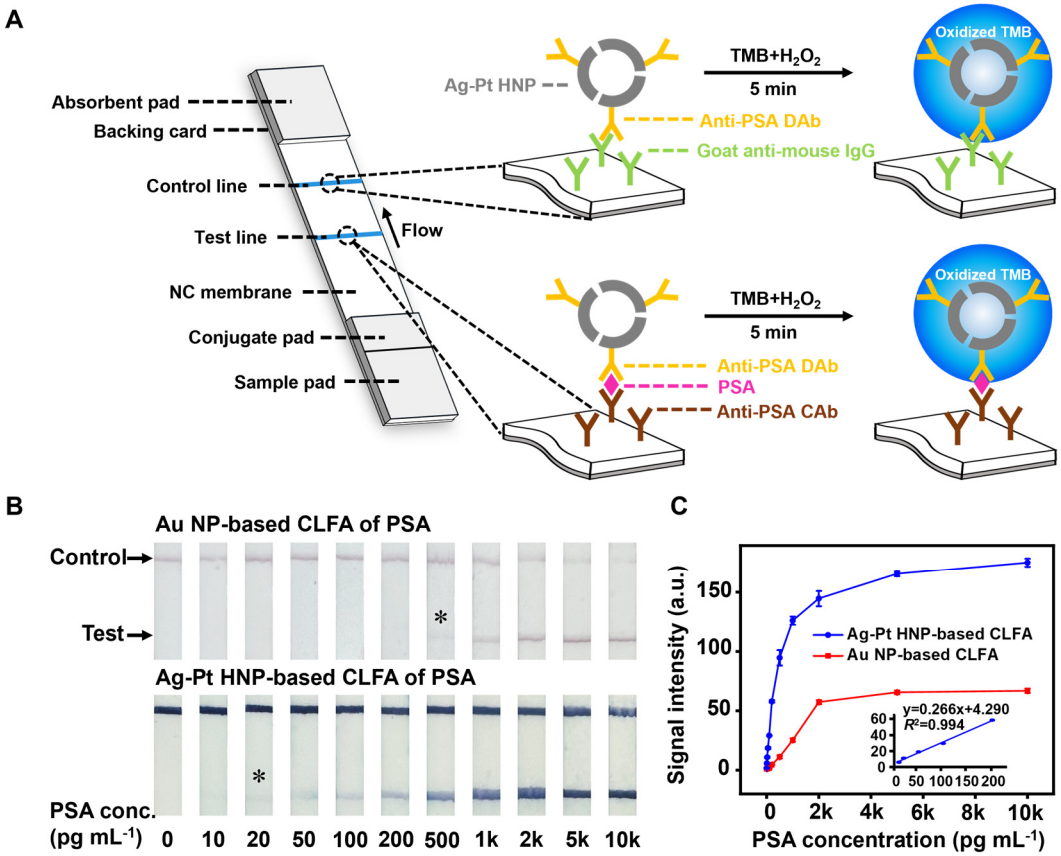

Figure 3. Ag-Pt HNP-based CLFA and conventional Au NP-based CLFA for detection of PSA. (**A**) Schematics illustrating the principle of Ag-Pt HNP-based CLFA. (**B**) Representative photographs of both CLFAs of PSA standards. Asterisks (*) indicate the detection limits by the naked eyes. (**C**) Corresponding calibration curves of the detection results shown in (**B**). Error bars denote standard deviations of six independent measurements. Inset shows linear range region of the Ag-Pt HNP-based CLFA.

PSA standards with concentrations ranging from 10 pg mL^{-1} to 10 ng mL^{-1} were detected by both the Ag-Pt HNP- and Au NP-based CLFAs. For quantitative analyses, the detection results were recorded with a digital camera (see Figure 3B). The color bands of the test line region were quantified using Adobe Photoshop software to generate the corresponding calibration curves (Figure 3C). For the Ag-Pt HNP-based CLFA, blue bands (originated from the oxidized TMB) at the test lines were visible to the naked eye at concentrations as low as 20 pg mL^{-1}. In contrast, the red bands (from the plasmonics of Au NPs) in Au NP-based CLFA could only be observed at PSA concentrations above 500 pg mL^{-1}. These results suggest the naked-eye detection limit of Ag-Pt HNP-based CLFA was about 25 times lower than that of Au NP-based CLFA. As shown by the calibration curves in Figure 3C, the Ag-Pt HNP-based CLFA exhibited a good linear correlation in 10–200 pg mL^{-1} PSA with an R^2 of 0.994. The limit of detection (LOD, which is defined by the 3SD method [35,36]) of the Ag-Pt HNP-based CLFA was determined to be 3.07 pg mL^{-1}, which was ~27 times lower than the LOD of Au NP-based CLFA (82.64 pg mL^{-1}, which was calculated based on its calibration curve).

These results demonstrate that the Ag-Pt HNPs with peroxidase-like activities can lower the detection limit of conventional Au NP-based CLFA by more than 20 times. Such a substantial improvement in CLFA sensitivity is only paid by a simple substrate treatment process at room temperature. Remarkably, the hollow structure and composition of Ag-Pt HNPs significantly reduce the usage amount of previous noble metals in CLFA, making the

Ag-Pt HNP-based CLFA cost-effective. Taken together, the Ag-Pt HNP-based CLFA outperforms conventional Au NP-based CLFA from the aspects of both sensitivity and cost effectiveness.

3.4. Demonstration of Clinical Use

We first assessed the influence of biological matrices on the performance of Ag-Pt HNP-based CLFA. To this end, we applied the CLFA to quantify PSA from spiked human serum samples. Note, serum is one of the most common types of clinical samples in medical diagnostics [37–39]. All serum samples were diluted 2-fold by assay buffer prior to the loading of sample onto test strip. Four spiked samples with final PSA concentrations in 25–150 pg mL^{-1} were prepared by spiking a PSA-free human serum sample (purchased from Sigma-Aldrich) with PSA standards. These samples were then detected by the Ag-Pt HNP-based CLFA. For quantitative analysis, the intensities of color signal at test lines of the CLFA strips were quantified and compared with the calibration curve shown in Supplementary Figure S5, from which the concentrations of PSA were determined. As summarized in Table 1, the analytical recoveries (which is defined as the PSA amount measured as a percentage of the PSA amount initially added to the serum) of the Ag-Pt HNP-based CLFA in detecting the four PSA-spiked serum samples were in the range of 94.81–102.92%. In addition, the coefficient of variation (n = 6) of all the spiked samples was ≤6.8%, indicating a good reproducibility of the CLFA test. These results demonstrated that the performance of Ag-Pt HNP-based CLFA was not significantly influenced by the biological matrices in human serum.

Table 1. Analytical recoveries of the Ag-Pt HNP-based CLFA in detection of PSA spiked human serum samples.

PSA Amount Spiked (pg mL^{-1})	PSA Amount Measured (pg mL^{-1})	Coefficient of Variations (%, n = 6)	Recovery (%)
25	24.00	4.37	96.00 ± 4.20
50	51.46	3.31	102.92 ± 3.19
100	97.88	5.51	97.88 ± 4.99
150	142.22	6.80	94.81 ± 6.45

Finally, to demonstrate the potential clinical use of Ag-Pt HNP-based CLFA, we used it for detecting PSA in a positive serum sample that was collected from a patient. This patient sample was purchased from Boca Biolistics (Pompano Beach, FL, USA, donor code #D106968). The sample was analyzed by a certified method (a commercial chemiluminescence immunoassay kit, Ortho-Clinical Diagnostics VITROS) to contain 0.5 ng mL^{-1} of PSA. We intended to determine whether the PSA concentration measured by our Ag-Pt HNP-based CLFA agrees with the "known concentration" (i.e., 0.50 ng mL^{-1}) within experimental error. To this end, we analyzed the sample six times (n = 6) by our CLFA and measured the PSA concentrations. The measured values were 0.51, 0.40, 0.42, 0.49, 0.52, and 0.43 ng mL^{-1} PSA, giving a mean of $\bar{x}$ = 0.46 and a standard deviation of s = 0.051. Based on these results, we performed the *Student's t* test [40]. Specifically, for six measurements, there are 5 degrees of freedom and thus $t_{95\%}$ = 2.57. The 95% confidence interval [which is expressed as $\bar{x} \pm ts/\sqrt{n}$] is calculated to be 0.46 ± 0.054. The known concentration (0.50 ng mL^{-1}) is within the 95% confidence interval. Therefore, we can conclude that the detection result from our CLFA (0.46 ng mL^{-1} PSA) agrees with the result from the commercial diagnostic kit (0.50 ng mL^{-1} PSA) within experimental error at a 95% confidence level. These results demonstrated the potential application of the Ag-Pt HNP-based CLFA in clinical settings. A more comprehensive assessment of the clinical performance of the CLFA using large-scale samples will be the subject of our future study.

4. Conclusions

In summary, we have demonstrated a sensitive and cost-effective CLFA. The CLFA relies on Ag-Pt HNPs as colorimetric labels. The Ag-Pt HNPs possess strong peroxidase-like catalytic activities, allowing them to produce sensitive color signals through catalysis. Moreover, the Ag-Pt HNPs have hollow interiors and are primarily made of less expensive silver, which effectively reduces materials cost of previous noble metals in CLFA. The Ag-Pt HNP-based CLFA was successfully applied to the detection of a cancer biomarker PSA, of which sensitivity was much higher than conventional solid Au NP-based CLFA. We believe the CLFA presented in this work as a sensitive and cost-effective point-of-care technology has great potential for diagnostic applications, especially in resource-limited settings.

Supplementary Materials: The following supporting information can be downloaded at: https://www.sciltp.com/journals/mi/2024/1/515/s1 , Figure 1: TEM image of citrate-capped silver nanoparticles (Ag NPs) with

an average diameter of 40.3 nm. These Ag NPs were used as sacrificial templates for the synthesis of Ag-Pt hollow nanoparticles (Ag-Pt HNPs) shown in Figure 1. Figure S2: Citrate-capped gold nanoparticles (Au NPs) with an average diameter of 40.8 nm. (A) A representative TEM image of the Au NPs. (B) An XPS spectrum recorded from the Au NPs. Figure S3: High-resolution XPS spectra of the C 1s and O 1s regions shown in Figure 1D. The peaks were analyzed and assigned according to the literature. Figure S4: UV-vis spectra recorded from 0.2 M NaOAc/HOAc buffer solution, pH 4.0, containing 0.8 mM TMB and 2.0 M H2O2 in the absence (#1) and presence (#2) of Ag-Pt HNPs (sample in Figure 1). Insets show the photographs of corresponding solutions. Figure S5: Calibration curve of the Ag-Pt HNP-based CLFA for detection of CEA standards in 1:1 (*v*/*v*) buffer/human serum mixture. Each data point in the plot represents an average of six independent measurements.

Author Contributions: J.Z.: conceptualization, methodology, data curation, writing-original draft preparation; S.S.: writing-reviewing and editing, validation; Z.W.: methodology; X.X.: supervision, conceptualization, writing-reviewing and editing. All authors have read and agreed to the published version of the manuscript.

Funding: This work was supported in part by the grants from the National Science Foundation (NSF) (DMR-2004546 and CBET-2234873) and U.S. Department of Agriculture (2020-67021-31257), and startup funds from the University of Central Florida (UCF).

Data Availability Statement: The data supporting this article have been included as part of the Supplementary Materials. Further data is available upon reasonable request from the authors.

Conflicts of Interest: There are no conflicts of interest to declare.

References

1. Budd, J.; Miller, B.S.; Weckman, N.E.; Cherkaoui, D.; Huang, D.; Decruz, A.T.; Fongwen, N.; Hanet, G.-R.; Broto, M.; Estcourt, C.S.; et al. Lateral Flow Test Engineering and Lessons Learned from COVID-19. *Nat. Rev. Bioeng.* **2023**, *1*, 13–31.
2. Liu, Y.; Zhan, L.; Qin, Z.; Sackrison, J.; Bischof, J.C. Ultrasensitive and Highly Specific Lateral Flow Assays for Point-of-Care Diagnosis. *ACS Nano* **2021**, *15*, 3593–3611.
3. Jiang, N.; Tansukawat, N.D.; Gonzalez-Macia, L.; Ates, H.C.; Dincer, C.; Guder, F.; Tasoglu, S.; Yetisen, A.K. Low-Cost Optical Assays for Point-of-Care Diagnosis in Resource-Limited Settings. *ACS Sens.* **2021**, *6*, 2108–2124.
4. Khlebtsov, B.N.; Tumskiy, R.S.; Burov, A.M.; Pylaev, T.E.; Khlebtsov, N.G. Quantifying the Numbers of Gold Nanoparticles in the Test Zone of Lateral Flow Immunoassay Strips. *ACS Appl. Nano Mater.* **2019**, *2*, 5020–5028.
5. Dzhagan, V.; Kapush, O.; Plokhovska, S.; Buziashvili, A.; Pirko, Y.; Yeshchenko, O.; Yukhymchuk, V.; Yemets, A.; Zahn, D.R.T. Plasmonic Colloidal Au Nanoparticles in DMSO: A Facile Synthesis and Characterisation. *RSC Adv.* **2022**, *12*, 21591–21599.
6. Yuan, Z.; Hu, C.C.; Chang, H.T.; Lu, C. Gold Nanoparticles as Sensitive Optical Probes. *Analyst* **2016**, *141*, 1611–1626.
7. Cui, X.; Huang, Y.; Wang, J.; Zhang, L.; Rong, Y.; Lai, W.; Chen, T. A Remarkable Sensitivity Enhancement in a Gold Nanoparticle-Based Lateral Flow Immunoassay for the Detection of *Escherichia coli* O157:H7. *RSC Adv.* **2015**, *5*, 45092–45097.
8. Gao, Z.; Ye, H.; Tang, D.; Tao, J.; Habibi, S.; Minerick, A.; Tang, D.; Xia, X. Platinum-Decorated Gold Nanoparticles with Dual Functionalities for Ultrasensitive Colorimetric In Vitro Diagnostics. *Nano Lett.* **2017**, *17*, 5572–5579.
9. Zhan, L.; Guo, S.Z.; Song, F.; Gong, Y.; Xu, F.; Boulware, D.R.; McAlpine, M.C.; Chan, W.C.W.; Bischof, J.C. The Role of Nanoparticle Design in Determining Analytical Performance of Lateral Flow Immunoassays. *Nano Lett.* **2017**, *17*, 7207–7212.
10. Ji, Y.; Ren, M.; Li, Y.; Huang, Z.; Shu, M.; Yang, H.; Xiong, Y.; Xu, Y. Detection of Aflatoxin B-1 with Immunochromatographic Test Strips: Enhanced Signal Sensitivity Using Gold Nanoflowers. *Talanta* **2015**, *142*, 206–212.
11. Ge, C.; Wu, R.; Chong, Y.; Fang, G.; Jiang, X.; Pan, Y.; Chen, C.; Yin, J.J. Synthesis of Pt Hollow Nanodendrites with Enhanced Peroxidase-like Activity against Bacterial Infections: Implication for Wound Healing. *Adv. Funct. Mater.* **2018**, *28*, 1801484.
12. Renzi, E.; Piper, A.; Nastri, F.; Merkoçi, A.; Lombardi, A. An Artificial Miniaturized Peroxidase for Signal Amplification in Lateral Flow Immunoassays. *Small* **2023**, *19*, 2207949.
13. Loynachan, C.N.; Thomas, M.R.; Gray, E.R.; Richards, D.A.; Kim, J.; Miller, B.S.; Brookes, J.C.; Agarwal, S.; Chudasama, V.; McKendry, R.A.; et al. Platinum Nanocatalyst Amplification: Redefining the Gold Standard for Lateral Flow Immunoassays with Ultrabroad Dynamic Range. *ACS Nano* **2018**, *12*, 279–288.
14. Wei, Z.; Luciano, K.; Xia, X. Catalytic Gold-Iridium Nanoparticles as Labels for Sensitive Colorimetric Lateral Flow Assay. *ACS Nano* **2022**, *16*, 21609–21617.
15. Jiang, B.; Duan, D.; Gao, L.; Zhou, M.; Fan, K.; Tang, Y.; Xi, J.; Bi, Y.; Tong, Z.; Gao, G.F.; et al. Standardized Assays for Determining the Catalytic Activity and Kinetics of Peroxidase-like Nanozymes. *Nat. Protoc.* **2018**, *13*, 1506–1520.

16. Gao, W.; Eastwood, H.; Xia, X. Peroxidase Mimics of Platinum-Group Metals for In Vitro Diagnostics: Opportunities and Challenges. *J. Mater. Chem. B* **2023**, *11*, 8404–8410.
17. Wei, Z.; Xi, Z.; Vlasov, S.; Ayala, J.; Xia, X. Nanocrystals of Platinum-Group Metals as Peroxidase Mimics for In Vitro Diagnostics. *Chem. Commun.* **2020**, *56*, 14962–14975.
18. Naseri, M.; Ziora, Z.M.; Simon, G.P.; Batchelor, W. ASSURED-Compliant Point-of-Care Diagnostics for the Detection of Human Viral Infections. *Rev. Med. Virol.* **2022**, *32*, e2263.
19. Bastús, N.G.; Merkoçi, F.; Piella, J.; Puntes, V. Synthesis of Highly Monodisperse Citrate-Stabilized Silver Nanoparticles of up to 200 nm: Kinetic Control and Catalytic Properties. *Chem. Mater.* **2014**, *26*, 2836–2846.
20. He, M.Q.; Ai, Y.; Hu, W.; Guan, L.; Ding, M.; Liang, Q. Recent Advances of Seed-Mediated Growth of Metal Nanoparticles: From Growth to Applications. *Adv. Mater.* **2023**, *35*, 2211915.
21. Gao, Z.; Ye, H.; Wang, Q.; Kim, M.J.; Tang, D.; Xi, Z.; Wei, Z.; Shao, S.; Xia, X. Template Regeneration in Galvanic Replacement: A Route to Highly Diverse Hollow Nanostructures. *ACS Nano* **2020**, *14*, 791–801.
22. Gao, Z.; Shao, S.; Gao, W.; Tang, D.; Tang, D.; Zou, S.; Kim, M.J.; Xia, X. Morphology-Invariant Metallic Nanoparticles with Tunable Plasmonic Properties. *ACS Nano* **2021**, *15*, 2428–2438.
23. Xia, X.; Zhang, J.; Lu, N.; Kim, M.J.; Ghale, K.; Xu, Y.; McKenzie, E.; Liu, J.; Ye, H. Pd-Ir Core-Shell Nanocubes: A Type of Highly Efficient and Versatile Peroxidase Mimic. *ACS Nano* **2015**, *9*, 9994–10004.
24. Gao, L.; Zhuang, J.; Nie, L.; Zhang, J.; Zhang, Y.; Gu, N.; Wang, T.; Feng, J.; Yang, D.; Perrett, S.; et al. Intrinsic Peroxidase-like Activity of Ferromagnetic Nanoparticles. *Nat. Nanotechnol.* **2007**, *2*, 577–583.
25. Lineweaver, H.; Burk, D. The Determination of Enzyme Dissociation Constants. *J. Am. Chem. Soc.* **1934**, *56*, 658–666.
26. Biby, A.; Crawford, H.; Xia, X. Platinum-Group Metal Nanoparticles as Peroxidase Mimics: Implications for Biosensing. *ACS Appl. Nano Mater.* **2022**, *5*, 17622–17631.
27. Lin, H.; Liu, Y.; Huo, J.; Zhang, A.; Pan, Y.; Bai, H.; Jiao, Z.; Fang, T.; Wang, X.; Cai, Y.; et al. Modified Enzyme-Linked Immunosorbent Assay Strategy Using Graphene Oxide Sheets and Gold Nanoparticles Functionalized with Different Antibody Types. *Anal. Chem.* **2013**, *85*, 6228–6232.
28. Glomm, W.R.; Halskau, Ø.; Hanneseth, A.-M.D.; Volden, S. Adsorption Behavior of Acidic and Basic Proteins onto Citrate-Coated Au Surfaces Correlated to Their Native Fold, Stability, and pI. *J. Phys. Chem. B* **2007**, *111*, 14329–14345.
29. Ye, H.; Xia, X. Enhancing the Sensitivity of Colorimetric Lateral Flow Assay (CLFA) through Signal Amplification Techniques. *J. Mater. Chem. B* **2018**, *6*, 7102–7111.
30. Josephy, P.D.; Eling, T.; Mason, R.P. The Horseradish Peroxidase-Catalyzed Oxidation of 3,5,3′,5′-tetramethylbenzidine. Free Radical and Charge-Transfer Complex Intermediates. *J. Biol. Chem.* **1982**, *257*, 3669–3675.
31. Gao, W.; Sun, X.; Yishay, T.; Wei, Z.; Zhu, X.; Kim, M.J.; Xia, X. Iridium Nanoparticles as Highly Effective Peroxidase Mimics: Synthesis, Characterization, and Application in Biosensing. *ChemNanoMat* **2024**, *10*, e202300589.
32. Liu, X.; Atwater, M.; Wang, J.; Huo, Q. Extinction Coefficient of Gold Nanoparticles with Different Sizes and Different Capping Ligands. *Colloids Surf. B Biointerfaces* **2007**, *58*, 3–7.
33. Stamey, T.A.; Yang, N.; Hay, A.R.; McNeal, J.E.; Freiha, F.S.; Redwine, E. Prostate-Specific Antigen as a Serum Marker for Adenocarcinoma of the Prostate. *N. Engl. J. Med.* **1987**, *317*, 909–916.
34. Palladino, P.; Torrini, F.; Scarano, S.; Minunni, M. 3,3′,5,5′-tetramethylbenzidine as Multi-Colorimetric Indicator of Chlorine in Water in Line with Health Guideline Values. *Anal. Bioanal. Chem.* **2020**, *412*, 7861–7869.
35. Armbruster, D.A.; Pry, T. Limit of Blank, Limit of Detection and Limit of Quantitation. *Clin. Biochem. Rev.* **2008**, *29*, S49–S52.
36. Armbruster, D.A.; Tillman, M.D.; Hubbs, L.M. Limit of Detection (LQD)/limit of Quantitation (LOQ): Comparison of the Empirical and the Statistical Methods Exemplified with GC-MS Assays of Abused Drugs. *Clin. Chem.* **1994**, *40*, 1233–1238.
37. Zerva, L.; Bourantas, K.; Mitka, S.; Kansouzidou, A.; Legakis, N.J. Serum is the Preferred Clinical Specimen for Diagnosis of Human Brucellosis by PCR. *J. Clin. Microbiol*. **2001**, *39*, 1661–1664.
38. Chen, X.; Ba, Y.; Ma, L.; Cai, X.; Yin, Y.; Wang, K.; Guo, J.; Zhang, Y.; Chen, J.; Guo, X. Characterization of MicroRNAs in Serum: A Novel Class of Biomarkers for Diagnosis of Cancer and Other Diseases. *Cell Res.*, **2008**, *18*, 997–1006.
39. Wegner, K.D.; Jin, Z.; Linden, S.; Jennings, T.L.; Hildebrandt, N. Quantum-Dot-Based Förster Resonance Energy Transfer Immunoassay for Sensitive Clinical Diagnostics of Low-Volume Serum Samples. *ACS Nano* **2013**, *7*, 7411–7419.
40. Harris, D.C. *Quantitative Chemical Analysis*, 9th Ed.; W.H. Freeman & Company: New York, NY, USA, 2016.